

First detection of ^{13}CH in the interstellar medium

Arshia M. Jacob¹, Karl M. Menten¹, Helmut Wiesemeyer¹, Rolf Güsten¹, Friedrich Wyrowski¹, and Bernd Klein^{1, 2}

¹ Max-Planck-Institut für Radioastronomie, Auf dem Hügel 69, 53121 Bonn, Germany
 e-mail: ajacob@mpi-fr-bonn.mpg.de

² University of Applied Sciences Bonn-Rhein-Sieg, Grantham-Allee 20, 53757 Sankt Augustin, Germany

Received 20 December 2019 / Accepted 1 July 2020

ABSTRACT

In recent years, a plethora of observations with high spectral resolution of sub-millimetre and far-infrared transitions of methyldene (CH), conducted with *Herschel* and SOFIA, have demonstrated this radical to be a valuable proxy for molecular hydrogen that can be used for characterising molecular gas within the interstellar medium on a Galactic scale, including the CO-dark component. We report the discovery of the ^{13}CH isotopologue in the interstellar medium using the upGREAT receiver on board SOFIA. We have detected the three hyperfine structure components of the ≈ 2 THz frequency transition from its $X^2\Pi_{1/2}$ ground-state towards the high-mass star-forming regions Sgr B2(M), G34.26+0.15, W49(N), and W51E and determined ^{13}CH column densities. The ubiquity of molecules containing carbon in the interstellar medium has turned the determination of the ratio between the abundances of the two stable isotopes of carbon, $^{12}\text{C}/^{13}\text{C}$, into a cornerstone for Galactic chemical evolution studies. Whilst displaying a rising gradient with galactocentric distance, this ratio, when measured using observations of different molecules (CO, H_2CO , and others), shows systematic variations depending on the tracer used. These observed inconsistencies may arise from optical depth effects, chemical fractionation, or isotope-selective photo-dissociation. Formed from C^+ either through UV-driven or turbulence-driven chemistry, CH reflects the fractionation of C^+ , and does not show any significant fractionation effects, unlike other molecules that were previously used to determine the $^{12}\text{C}/^{13}\text{C}$ isotopic ratio. This makes it an ideal tracer for the $^{12}\text{C}/^{13}\text{C}$ ratio throughout the Galaxy. By comparing the derived column densities of ^{13}CH with previously obtained SOFIA data of the corresponding transitions of the main isotopologue ^{12}CH , we therefore derive $^{12}\text{C}/^{13}\text{C}$ isotopic ratios toward Sgr B2(M), G34.26+0.15, W49(N) and W51E. Adding our values derived from $^{12}/^{13}\text{CH}$ to previous calculations of the Galactic isotopic gradient, we derive a revised value of $^{12}\text{C}/^{13}\text{C} = 5.87(0.45)R_{\text{GC}} + 13.25(2.94)$.

Key words. line: identification – molecular data – molecular processes – ISM: molecules – evolution

1. Introduction

The methyldene radical CH has received widespread attention as a general probe of diffuse and translucent interstellar clouds and in particular as a surrogate for the H_2 column density determinations in such environments (e.g. [Federman 1982](#); [Sheffer et al. 2008](#), and references therein). CH has been observed in widely different wavelength regimes, from the radio at 9 cm ([Rydbeck et al. 1973](#)) to the sub-millimetre (sub-mm) and far-infrared (FIR) ranges, at $560\ \mu\text{m}$ ([Gerin et al. 2010](#)) and $150\ \mu\text{m}$ ([Stacey et al. 1987](#); [Wiesemeyer et al. 2018](#)) and the optical ($4300.3\ \text{\AA}$, e.g. [Danks et al. 1984](#); [Sheffer et al. 2008](#)) into the far-ultraviolet (FUV) regimes ($1369.13\ \text{\AA}$, [Watson 2001](#)). The famous $4300.3\ \text{\AA}$ CH transition was one of the first three molecular lines that were detected in the interstellar medium (ISM; [Dunham 1937](#); [Swings & Rosenfeld 1937](#)). While an abundance of ^{12}CH data exists, very little is known about its rarer isotopologue ^{13}CH . Unlike its parent molecule, which is ubiquitously distributed in the ISM, the only known astronomical identification of ^{13}CH has been made in the solar spectrum by [Richter & Tonner \(1967\)](#). As for the ISM, [Bottinelli et al. \(2014\)](#) reported the non-detection of the $N, J = 1, 1/2 \rightarrow 1, 3/2$ and $N, J = 1, 3/2 \rightarrow 2, 5/2$ transitions of ^{13}CH towards the well-studied low-mass protostellar condensation IRAS 16293–2422.

The $^{12}\text{C}/^{13}\text{C}$ ratio has been widely studied towards molecular clouds in the Milky Way (e.g. [Henkel et al. 1982, 1994](#); [Steimle et al. 1986](#); [Wilson & Rood 1994](#)) and recently, also in the nuclear regions of nearby starburst galaxies ([Tang et al. 2019](#)).

It is an important diagnostic tool for probing Galactic chemical evolution or simply the nucleosynthesis history of the Galaxy. ^{12}C is synthesised as the primary product of shell and core He-burning in intermediate- and high-mass stars through the triple- α reaction, while ^{13}C is a secondary product of stellar nucleosynthesis and is produced over longer timescales. It is predominantly formed as a by-product of the carbon-nitrogen-oxygen (CNO) cycle in asymptotic giant branch (AGB) stars. Initiated by the proton capture of the ^{12}C nucleus produced from an older stellar population, the CNO-cycle forms ^{13}N , which then decays through positron emission to form the ^{13}C nucleus ($^{12}\text{C}(\text{p}, \gamma)^{13}\text{N}(\beta^+)^{13}\text{C}$) ([Pagel 1997](#)). The ^{13}C intermediate product is injected into the ISM by mass loss of the AGB stars, after the ashes of the helium-burning shell of these objects have intermixed with their convective envelopes in the third dredge-up ([Herwig 2005](#)). This establishes the $^{12}\text{C}/^{13}\text{C}$ isotopic ratio as a measure of the degree of astration present in the Galaxy. Chemical evolution models of the Galaxy ([Tosi 1982](#); [Prantzos et al. 1996](#)) have predicted the $^{12}\text{C}/^{13}\text{C}$ ratio to exhibit a positive gradient, increasing with galactocentric distances and decreasing with time.

The predictions of these models have been confirmed by observational measurements of the $^{12}\text{C}/^{13}\text{C}$ isotopic ratio that were carried out by studying the rotational transitions of molecules such as H_2CO ([Henkel et al. 1982](#)), CO ([Langer & Penzias 1990](#)), and CN ([Milam et al. 2005](#)) and of their respective ^{13}C isotopologues at centimetre and millimetre wavelengths. At these wavelengths the lines from the isotopologues of these

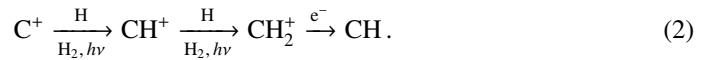
species are well separated, unlike in the optical regime (except for $^{12/13}\text{CH}^+$; see Ritchey et al. 2011). While the average fit to the $^{12}\text{C}/^{13}\text{C}$ gradients derived independently using the three molecules mentioned above agree within the quoted error bars, their individual trends display systematic variations amongst themselves. The reasons for these variations may be related to the observations of the different tracers and/or to isotope-selective chemical processes such as gas-phase fractionation and selective photo-dissociation, which do not affect every molecule in the same way. Chemical fractionation occurs as a result of ion-molecule exchange reactions that preferentially transfer and incorporate the heavier atomic isotopes into molecules due to differences in zero-point energies between the different isotopes (see e.g. Wilson 1999; Roueff et al. 2015). Isotopic fractionation does not affect all molecules in the same way as its degree greatly depends upon the formation pathway of the molecule and the environment in which it is formed and exists. In molecules that are susceptible to fractionation, such as CO, the chemical fractionation enriches the ^{13}C isotope and lowers the $^{12}\text{C}/^{13}\text{C}$ ratio, but it is increased by the selective photo-dissociation of the rarer isotopic species containing ^{13}C because its self-shielding in regions with a high UV flux is weaker (Bally & Langer 1982). In such regions, the $^{12}\text{CO}/^{13}\text{CO}$ ratio might therefore be higher than the underlying $^{12}\text{C}/^{13}\text{C}$ ratio. In denser regions where carbon exists mostly in the form of CO, ^{13}C is locked up in CO and is depleted in other carbon-bearing molecules (Roueff et al. 2015). Precise measurements of the $^{12}\text{C}/^{13}\text{C}$ isotopic ratio have also been made using observations of the $\text{CH}^+ A - X(0, 0)$ transition near 4232 Å (Ritchey et al. 2011), but their observations are limited to nearby stars (<7 kpc) that are bright ($V < 10$ mag) in the visible wavelength range. The corresponding sub-millimetre transitions of CH^+ are often optically thick with saturated absorption profiles and can only yield lower limits on the carbon isotopic ratio (Falgaron et al. 2010). Hence, the high optical depths of many abundant ^{12}C -bearing molecules and effects of saturation and self-absorption pose a problem when the intensities of these lines are used, which in turn skews estimates of the $^{12}\text{C}/^{13}\text{C}$ ratio. In an attempt to provide additional constraints on the $^{12}\text{C}/^{13}\text{C}$ ratio, we here propose the use of a new tracer: CH.

CH is expected to be a good candidate for conducting isotopic ratio measures because it is an abundant species that is ubiquitously formed in the ISM, and because its spectral lines are optically thin. Quite remarkably, this is generally true for radio, sub-millimetre, FIR, and optical CH lines, except for the ground-state rotational sub-millimetre/FIR transitions near 533/536, and 2006/2010 GHz, which reach optical depths that exceed unity in absorption from the envelopes of SFRs; see for example our Fig. 2. In particular, the hyperfine structure (hfs) components of the $N, J = 1, 1/2 \rightarrow 2, 3/2$ transitions of CH near 2 THz have recently been observed in generally unsaturated absorption, which is ideal for column density determinations (Wiesemeyer et al. 2018; Jacob et al. 2019). Models and simulations by Röllig & Ossenkopf (2013) for photo-dissociation regions (PDRs) show that the fractionation present in CH is dominated by the fractionation of its parental species. CH originates from C^+ and is formed through the dissociative recombination of CH_3^+ ,



Hence, the degree of fractionation in CH is closely coupled with that of C^+ . Ossenkopf et al. (2013) have studied the fractionation of C^+ by comparing model predictions with high-resolution

observations of the fine-structure lines of ^{12}CII and ^{13}CII using HIFI/Herschel. These authors find that, at low visual extinctions, A_V , the isotopic fractionation ratio of C^+ is comparable to the elemental abundance ratio, but it increases with A_V at low gas temperatures by typically a factor of ~ 2 at most. This is a consequence of the enrichment of ^{13}C in CO in these regions (favouring the forward reaction of the $\text{C}^+ - \text{CO}$ ion-molecule exchange reaction; Langer & Penzias 1990), which results in the depletion of $^{13}\text{C}^+$ and all subsequent species such as ^{13}CH that are formed from it. In addition, the abundance of CH is often enhanced through hydrogen abstraction reactions of CH^+ , which is formed endothermically ($\Delta E/k_B = 4620$ K) (Hierl et al. 1997), in shocks, or in the dissipation of turbulence (Godard et al. 2014), followed by the dissociative recombination of CH_2^+ :



Because it is formed at high effective temperatures through non-thermal processes, CH^+ is not affected by fractionation and is believed to reflect the ambient C-isotopic ratio in the diffuse ISM. In low A_V diffuse clouds, where turbulence-driven reactions are favoured, CH, like its parent CH^+ , is therefore not affected by fractionation. The abundance ratio of the CH isotopologues accordingly does not deviate from the elemental ratio of the atomic carbon isotopes.

As mentioned above, optical and UV absorption studies of CH require visually bright early-type stars as background whose light is unhampered by interstellar extinction (Federman 1982; Sheffer et al. 2008). Owing to this, they can only probe the ISM in the solar neighbourhood out to a few kiloparsec. In contrast, we observe supra-terahertz transitions of CH and ^{13}CH in absorption against the bright dust emission of far away star-forming regions (SFRs) out to the Galactic centre (GC) and beyond. Thus our absorption spectra not only probe the molecular envelopes of these sources, but also the diffuse and translucent interstellar clouds along their lines of sight over a wide range of galactocentric radii. Moreover, because of the differential rotation of the Galaxy, the absorption covers wide ranges in local standard of rest (LSR) velocity. As a caveat, we mention that because first, the expected $^{12}\text{CH}/^{13}\text{CH}$ ratios, which range from ≈ 20 in the GC to ≈ 90 at the solar circle and to even higher values beyond (Wilson & Rood 1994, and references therein), and second, because even ^{12}CH lines are predominantly optically thin, we expect a detection of ^{13}CH absorption only towards the LSR velocities of the SFRs studied because these sources have far greater column densities than the intervening diffuse clouds along their lines of sight. We present our search for ^{13}CH in the ISM along the line of sight (LOS) towards five high-mass SFRs in the Milky Way, Sgr B2(M), G34.26+0.15, W49(N), W51E, and W3(OH) and discuss its use as an unbiased tool for benchmarking the $^{12}\text{C}/^{13}\text{C}$ Galactic gradient.

2. ^{13}CH spectroscopy

Similar to CH, ^{13}CH conforms to Hund's case-b coupling, but differs in the nuclear spin, I , of the carbon atom, $I(^{12}\text{C}) = 0$ and $I(^{13}\text{C}) = 0.5$. Because of the non-zero nuclear spin of the ^{13}C isotope, the total angular momentum J first couples with $I_1(^{13}\text{C})$ to generate $F_1 (= J + I_1)$, which further couples with the nuclear spin of the H atom, $I_2(\text{H}) = 0.5$ to yield $F (= F_1 + I_2)$. The energy level diagram of the ^{13}CH Λ -doublet transitions that are discussed in this study are displayed in Fig. 1. Considerable effort has been expended in the laboratory to measure the

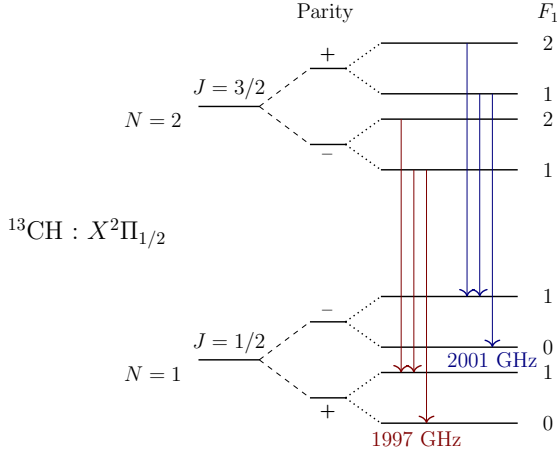


Fig. 1. Energy-level diagram of the lower rotational levels of ^{13}CH . The hyperfine transitions of ^{13}CH that are presented in this study are highlighted using red and blue arrows. The proton hyperfine structure splittings are not included. The level separations are not to scale.

Table 1. Spectroscopic parameters for the $N, J = 2, 3/2 \rightarrow 1, 1/2$ hyperfine structure transitions of ^{13}CH .

Parity	Transition $F'_1, F' \rightarrow F''_1, F''$	Frequency [GHz]	S	$A_E \times 10^{-3}$ [s $^{-1}$]
+ \rightarrow -	1, 3/2 \rightarrow 0, 1/2	1997.4232	0.3331	1.1458
	1, 3/2 \rightarrow 1, 3/2	1997.4464	0.1666	0.5731
	2, 5/2 \rightarrow 1, 3/2	1997.4437	0.8327	1.9096
- \rightarrow +	1, 3/2 \rightarrow 0, 1/2	2001.5672	0.3345	1.1577
	1, 3/2 \rightarrow 1, 3/2	2001.2230	0.1673	0.5787
	2, 5/2 \rightarrow 1, 3/2	2001.3673	0.8365	1.9296

Notes. Taken from Davidson et al. (2004).

rotational spectrum of ^{13}CH . The spectroscopic parameters of the rotational transitions of the ^{13}CH radical between the $X^2\Pi$ ground state have been measured using the technique of laser magnetic resonance (LMR) at FIR wavelengths by Davidson et al. (2004). The results of their experiments were combined with previously determined Λ -doublet intervals of the molecule by Steimle et al. (1986) to provide accurate predictions of the transition frequencies between the low-lying rotational levels and the ground state. The spectroscopic parameters of the observed $N, J = 2, 3/2 \rightarrow 1, 1/2$ transitions are tabulated in Table 1. The Einstein A coefficients, $A_{E,ij}$, were computed from the line strengths, S_{ij} , using the relation

$$A_{E,ij} = (16\pi^3 \nu_{ij}^3 / 3\epsilon_0 h c^3) (2F_i + 1)^{-1} S_{ij} \mu^2 \quad (3)$$

for spontaneous emission from an energy level i to j . Here ν_{ij} is the corresponding frequency, F_i is the total hyperfine quantum number of level i , and μ represents the electric dipole moment of ^{13}CH , $\mu(^{13}\text{CH}) = 1.46$ Debye (Pickett et al. 1998).

3. Observations

Using the upGREAT instrument¹ (Risacher et al. 2016) on board SOFIA (Young et al. 2012), we observed the

¹ The German REceiver for Astronomy at Terahertz frequencies (GREAT) is a development by the MPI für Radioastronomie and the KOSMA/Universität zu Köln, in cooperation with the DLR Institut für Optische Sensorsysteme.

$^2\Pi_{1/2} N, J = 2, 3/2 \rightarrow 1, 1/2$ Λ -doublet transitions of ^{13}CH over several flight series as a part of the observatory's cycle 7 campaign (under the open time project 07_0148 supplemented by guaranteed time observations). In this pilot study we carried out observations towards five well-known SFRs Sgr B2(M), G34.26+0.15, W49(N), W51E, and W3(OH). Because so far, ^{13}CH has never been detected in the ISM before, the primary source selection criterion was the existence of a strong sub-millimetre and FIR background continuum. Secondly, we selected sources that are almost evenly spaced in galactocentric distance between the GC and the solar circle in order to obtain quantitative constraints on the Galactic $^{12}\text{C}/^{13}\text{C}$ abundance ratio gradient. Observational properties of the different sources are summarised in Table 2. The receiver configuration comprises the (7+7) pixel low-frequency array (LFA) receiver module of upGREAT in dual polarisation. Only data from the central pixels were used because the continuum targets are unresolved in our 13.5'' full width at half maximum (FWHM) beam (scaled with frequency from the nominal 14.1'' beam width at the $[\text{C II}]$ 158 μm line). The spectra were taken in the double-beam switch mode, chopping at a frequency of 2.5 Hz with a chop throw between 210'' and 240'' and a chop angle of 90° (counter-clockwise against north) to account for atmospheric fluctuations and fluctuations that may arise from the instrument. The receiver was connected to an evolved version of the MPIfR fast Fourier transform spectrometer described by Klein et al. (2012). This backend provides 4 GHz bandwidth per pixel and a velocity resolution of 0.036 km s $^{-1}$ (~ 244.1 kHz) over 16 384 channels. In this detection experiment, the double-sideband (DSB) receiver was tuned to 1997.4437 GHz (the strongest hfs transition of the 1997 GHz Λ -doublet) in the lower sideband. Three different intermediate-frequency (IF) settings were used in our observations in order to distinguish any contamination present in the bandpass towards all sources except for W3(OH), towards which we used only a single IF setting at 1.45 GHz in our pilot search. For G34.26+0.15, W49(N), and W51E, the IF was tuned to 1.2, 1.4, and 1.6 GHz, while for Sgr B2(M), the IF was tuned to 1.4, 1.6, and 1.8 GHz. The ^{13}CH spectra obtained along the LOSs to Sgr B2(M), G34.26+0.15, W49(N), and W51E taken with each of the three IF settings are displayed in Appendix A. The spectra were further calibrated using the KALIBRATE program (Guan et al. 2012) and a forward efficiency of 0.97. Fluctuations of the continuum level can either be due to telescope-tracking problems or due to gain drifts in the mixers. From a comparison between the continuum fluxes in the high-frequency array, operated in parallel at 4.7 THz and offering a 6'' FWHM beam, we can rule out the former (which even if they occurred would not affect the line-to-continuum ratio). Gain drifts that are faster than the calibration rate, however, affect the measurement of the atmospheric total power and therefore the applied transmission correction. Because they potentially distort the line-to-continuum ratio, a new calibration strategy was applied to analyse the gain fluctuations of the GREAT receiver, thanks to the larger amount of data now available. In a first step, the most stable off-centre pixels were identified by monitoring the line areas of a simultaneously observed narrow telluric ozone line, which is largely insensitive to baseline uncertainties. Because the atmospheric emission arises in the near-field of all pixels, they must all see the same ozone line flux. From this correlation analysis, only the pixel pairs whose line flux ratios were persistently close to unity were retained to determine the atmospheric transmission correction. The quality of the correlation analysis was ensured by forming closure products of the gain ratios, including those of the central pixel used (which for our case deviates from unity

Table 2. Continuum source parameters.

Source	α (J2000) [h:m:s]	δ (J2000) [°:′:″]	v_{LSR} [km s ⁻¹]	T_c [K]	R_{GC} [kpc]	D [kpc]	Flight Id	$t_{\text{obs}}^{(a)}$ [mins]
Sgr B2(M)	17:47:20.49	−28:23:06.00	65.2(0.6)	14.6	0.1	8.3	2019/06/10(F579)	51
							2019/06/11(F580)	101
W51E	19:23:43.90	+14:30:30.50	63.0(1.6)	9.4	6.3	5.4	2019/12/11(F646)	90
G34.26+0.15	18:53:18.49	+01:14:58.70	58.0(0.7)	8.6	7.0	1.6	2020/03/07(F669)	126
							2020/03/11(F671)	85
W49(N)	19:10:13.20	+09:06:11.88	11.8(0.4)	13.8	7.8	11.4	2020/03/05(F667)	80
							2020/03/10(F670)	55
							2020/03/12(F673)	135
							2020/03/13(F674)	57
W3(OH)	02:27:04.10	+61:52:22.00	−46.0(0.2)	5.3	10.0	2.0	2018/11/21(F529)	117
							2018/12/04(F533)	53

Notes. Columns are from left to right, the source designation, equatorial coordinates, LSR velocity, signal band continuum brightness temperature derived by means of a DSB calibration, galactocentric distance, heliocentric distance, flight id, and flight leg duration. ^(a)The observing leg time (t_{obs}) refers to the total duration of time for which the source was observed. This includes the total (on+off) observing time as well as the overheads, which in total is typically a factor of two larger than the (on+off) time.

References. The heliocentric distances: Sgr B2(M): Reid et al. (2014); W51E: Sato et al. (2010); G34.26+0.15: Zhang et al. (2009); W49(N): Zhang et al. (2013); W3(OH): Xu et al. (2006);

by 1.6% at most). In order to eliminate spectra in the central pixel that are affected by gain drifts, only data with closure products deviating from unity by 0.4% at most were retained to determine the continuum level. The DSB-continuum level was then determined by accounting for contributions from the signal and image bands, which was added back to the spectra to obtain the correct line-to-continuum ratio. This calibration technique was applied not only to the ¹³CH data presented in this work, but also to the previously published ¹²CH data (Wiesemeyer et al. 2018; Jacob et al. 2019), which thus were re-calibrated for use in our analysis to avoid any inconsistencies. For the ¹²CH spectra, we note that the continuum levels derived using the closure products are compatible with those derived using the standard calibration methods, except for W49(N). Using the closure product analysis, we derived a continuum level of 14 K for the ¹²CH spectrum towards W49(N) that agrees with the continuum level cited by Wiesemeyer et al. (2018) within a 20% uncertainty. It is to be noted that in the analysis that follows, we adopt a value of 14 K as the continuum level of the ¹²CH spectrum towards W49(N).

Subsequently, the fully calibrated spectra obtained from the two polarisations of the central pixel were converted into a main-beam brightness temperature scale (using a main-beam efficiency of 0.66) and analysed using the GILDAS-CLASS software². The spectra were box-smoothed to ~ 1.1 km s⁻¹ wide velocity bins, and the spectral baselines were corrected for by removing up to a second-order polynomial. The resulting spectra obtained after carrying out a simple sideband deconvolution (discussed in Appendix A) are displayed in Figs. 2 and 3. On average, we achieved a noise level of ~ 68 mK at a velocity resolution of 1.1 km s⁻¹ after the sideband deconvolution. In the following paragraphs we briefly describe the LOS properties of the observed ¹³CH spectra and compare them with previously obtained CH spectra.

Sgr B2(M). The unwavering nature of the absorption feature at $v \sim 64$ km s⁻¹ observed towards the envelope of Sgr B2(M) in each of the different IF frequency settings

² Software package developed by IRAM, see <https://www.iram.fr/IRAMFR/GILDAS/> for more information regarding GILDAS packages.

and the detection of its image band Λ -doublet counterpart near 2001 GHz with the absorption features displaying their expected relative intensities solidifies our detection of ¹³CH near 1997.44 GHz at this velocity. We compare the ¹³CH spectrum with that of CH towards Sgr B2(M) published in Jacob et al. (2019). The CH spectrum has a true continuum of 15 K and is contaminated by C₃ absorption at 2004.833 GHz arising from the image band, as indicated by the blue box in Fig. 2. The similarities between the CH and ¹³CH spectra suggest the presence of weak blue-shifted sight-line absorption features in addition to the deep absorption seen near 64 km s⁻¹ corresponding to the systemic LSR velocity of the molecular cloud. The shift of the atmospheric ozone feature at 2002.347 GHz in the image band towards the signal band features, by 60 km s⁻¹ with each 0.2 GHz IF offset, leads to uncertainties while fitting polynomial baselines, particularly for the weaker features. The true nature of the sight-line absorption features therefore remains uncertain because of calibration and baseline uncertainties for the broad blended features. We will follow this up in future observations.

G34.26+0.15. In order to avoid the blending of the atmospheric ozone feature from the image band with the signal band features, we used an IF setting of 1.2 GHz instead of 1.8 GHz. Similar to the ¹³CH spectrum observed towards Sgr B2(M), we see absorption at the systemic velocity of the G34.26+0.15 molecular cloud at 58 km s⁻¹ in all three IF settings. However, we do not clearly detect ¹³CH in foreground gas at velocities between 0 and 50 km s⁻¹.

W49(N). We used a setup similar to what we used for our observations towards G34.26+0.15 for those toward W49(N). In addition to ¹³CH absorption at the velocities corresponding to the velocity of the molecular cloud, we see a weaker absorption feature close to 65 km s⁻¹, associated with the far-side crossing of the Sagittarius spiral arm. However, we do not include this feature in the analysis that follows because of its low signal-to-noise ratio.

W51E. By choosing the 1.4 GHz IF tuning as the nominal setting for carrying out the DSB deconvolution, we observe

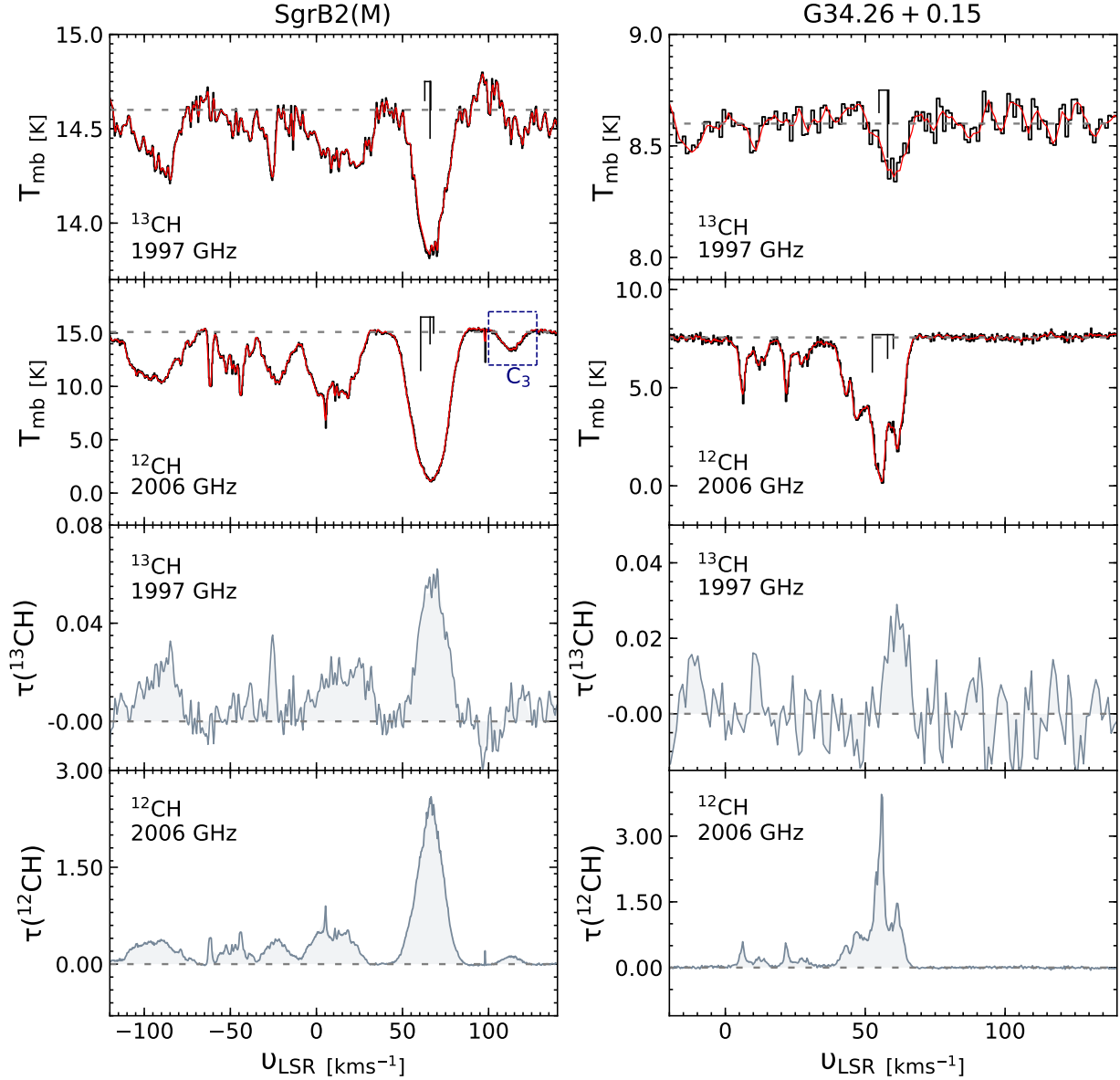


Fig. 2. From top to bottom: $N, J=2, 3/2 \rightarrow 1, 1/2$ transition spectra of ^{13}CH and CH near 1997 and 2006 GHz, in black with their corresponding Wiener filter fits to the spectra overlaid in red towards Sgr B2(M) (left) and G34.26+0.15 (right). Followed by their Wiener filter deconvolved spectra displayed in grey in optical depth scales. The ^{12}CH spectrum towards Sgr B2(M) is contaminated by C_3 absorption at 2004.833 GHz in the image band, as indicated in blue.

^{13}CH absorption at the source intrinsic velocity of W51E near $\sim 62 \text{ km s}^{-1}$. When we compare this with the corresponding ^{12}CH spectrum, which closely resembles that of the $^2\Pi_{3/2}, J=3/2 \rightarrow 5/2$ SH line at 1383.2 GHz, between 43–80 km s^{-1} (Neufeld et al. 2015), it is not clear whether ^{13}CH shows a second absorption component at 53 km s^{-1} at the given noise level. The weaker and narrower absorption seen at 26 km s^{-1} is merely a remnant feature from the image band.

Towards W3(OH) no ^{13}CH lines are detected above the noise (77 mK at a spectral resolution of 1.1 km s^{-1}) in the spectrum at a continuum level of 5.3 K. The baseline-subtracted CH and ^{13}CH spectra towards W3(OH) are displayed in Appendix B.1. The corresponding CH spectrum is taken from Wiesemeyer et al. (2018) and has a continuum level at 5.4 K, prior to baseline removal.

Additionally, we verified whether the $^{12}\text{C}/^{13}\text{C}$ ratios derived by us are consistent with values derived using archival

HIFI/Herschel data of the $N, J=1, 3/2 \rightarrow 1, 1/2$ transitions of CH and ^{13}CH near 532 GHz. While the 532 GHz CH line displays a deep absorption feature at the systemic velocity of the Sgr B2(M) molecular cloud with a peak temperature of 1.64 K (Qin et al. 2010), the corresponding ^{13}CH transition is not detected above a 3σ noise level of 0.33 K (at a spectral resolution of 0.5 km s^{-1}) and yields a lower limit of 5 on the $^{12}\text{C}/^{13}\text{C}$ isotopic ratio. Similarly, we analysed the 532 GHz CH spectra taken towards G34.26+0.15 discussed in Godard et al. (2012), W49(N) and W51E presented in Gerin et al. (2010), and W3(OH) from the Herschel archives³ that also cover the corresponding ^{13}CH line frequencies. We find no signatures of ^{13}CH , and from the 3σ noise levels, we are only able to derive lower limits to the $^{12}\text{C}/^{13}\text{C}$ ratio of 13, 32, 17, and 68 for the above sources. We mention that

³ See, <http://archives.esac.esa.int/hsa/whsa/>

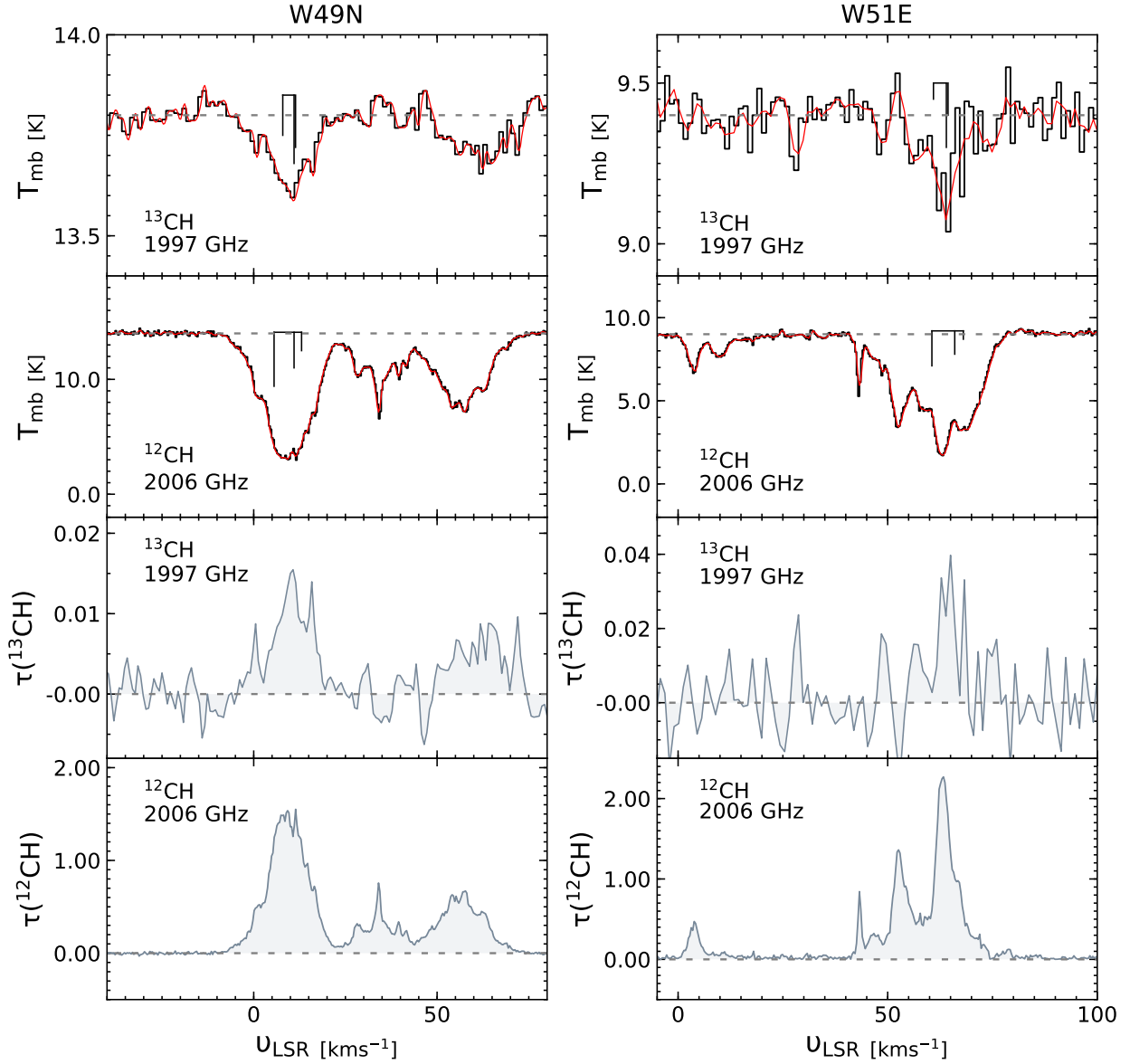


Fig. 3. Same as Fig. 2, but towards W49(N) (*left*) and W51E (*right*).

in contrast to the 2 THz lines, in the 532 GHz line, the molecular cores associated with these massive SFRs show complex line profiles with both emission and absorption components. In addition, the intensities and profiles of the ^{13}CH lines are quite uncertain as their HIFI spectra are affected by a standing wave and an unknown (and not yet assessed) level of potential line contamination. Thus the formal lower limits for the $^{12}\text{C}/^{13}\text{C}$ ratio derived from archival HIFI/*Herschel* data quoted above should be regarded with some caution.

4. Analysis and discussion

High-resolution absorption line spectroscopy provides a powerful and straightforward to use tool for measuring column densities. The optical depth, τ , for a single absorption component can be calculated from the line to continuum ratio using

$$\tau = -\ln(T_1/T_c), \quad (4)$$

where T_1 and T_c represent the observed brightness temperatures of the line (prior to continuum subtraction) and the continuum,

respectively. We determined the optical depth profile, that is, τ versus v_{LSR} , using the Wiener filter fitting technique as described in [Jacob et al. \(2019\)](#). This fitting procedure first fits the observed spectral profile by minimising the mean square error between the model and observations and then deconvolves the hyperfine structure from the observed spectrum using the relative weights of the hfs components. Other than the observed spectrum and the spectroscopic parameters of the line to be fit, the only other input parameter required by the Wiener filter technique is the spectral noise, which is assumed to be independent of the observed signal. The resulting deconvolved optical depth signature, τ_{decon} , can then be converted into column density values per velocity channel, i using

$$\left(\frac{dN}{dv}\right)_i = \frac{8\pi\nu_i^3}{c^3} \frac{Q_{\text{rot}}}{g_u A_E} \exp\left(\frac{E_u}{T_{\text{ex}}}\right) \left[\exp\left(\frac{h\nu_i}{k_B T_{\text{ex}}}\right) - 1 \right]^{-1} (\tau_{\text{decon}})_i, \quad (5)$$

where the spectroscopic parameters g_u (the upper level degeneracy), E_u (the upper level energy), and A_E (the Einstein A coefficient) remain constant for a given hyperfine transition. The partition function, Q , is itself a function of the rotation

temperature, T_{rot} , which would be equal to the excitation temperature, T_{ex} , under conditions of local thermodynamic equilibrium (LTE). Typically, the rotational transitions of hydrides require high critical densities to be observable in emission. Because collisional rate coefficients are currently not available for ^{13}CH , we assumed the critical density of this ^{13}CH line to be identical to the critical density of the corresponding CH transition, assuming a two-level system. Using hfs resolved collisional rate coefficients computed by Dagdigan (2018), we find the critical densities to be $\sim 2 \times 10^9 \text{ cm}^{-3}$ at 50–100 K. Within the diffuse and translucent interstellar clouds along the LOS ($n = 10\text{--}500 \text{ cm}^{-3}$) and the envelope of Sgr B2(M) (ranging from $n \sim 10^3\text{--}10^5 \text{ cm}^{-3}$; Schmiedeke et al. 2016), the gas densities are much lower than the critical density, n_{crit} , of these transitions, making them sub-thermally excited. Hence we can assume the excitation temperature of such sub-thermally excited lines to be low and lower than the gas kinetic temperature. In our analysis we assume T_{rot} to be equal to the temperature of the cosmic microwave background (CMB) radiation, $T_{\text{CMB}} = 2.728 \text{ K}$ (Neill et al. 2014). Because of this low rotation temperature and the inefficiency of purely collisional excitation, almost all of the CH molecules will reside in the ground-state level of the molecule. However, in the SFRs, radiative excitation by FIR dust radiation can affect the level populations (see Neufeld et al. 1997 for the case of HF). Meaningful modelling of this is beyond the scope of the present study. In any case, because the ^{12}CH and ^{13}CH lines under consideration here have moderate and low optical depths, respectively, radiative excitation is expected to affect the observed transitions from both isotopologues in a similar way, leaving the $^{12}\text{CH}/^{13}\text{CH}$ intensity ratio unaltered.

With the knowledge of the frequency separation of the hfs transitions of ^{13}CH , we first deconvolved the hyperfine structure from the observed spectra using the Wiener filter formalism (briefly discussed above) and then derived column densities by adopting a T_{ex} value equal to T_{CMB} and integrating over the deconvolved velocity range of the line. We derive ^{13}CH column densities between $\sim 2 \times 10^{12}$ and $4.6 \times 10^{13} \text{ cm}^{-2}$ towards the different sources. Given that the optical depths are computed directly from the line-to-continuum ratio, the uncertainties in the true continuum level give rise to systemic errors in the derived column densities. We assumed a 10% error in the continuum level calibration based on the instrumental performance (Kester et al. 2017) and sideband dependence of the atmospheric transmission. The subsequently derived errors in the column densities (per velocity interval) were computed following the description presented in Jacob et al. (2019) and scale with the deconvolved optical depths by a constant term comprised of the spectroscopic parameters that govern the transition and the excitation temperature. We compare the ^{13}CH column densities derived here, over velocity intervals associated with the different molecular clouds, with those of their corresponding $N, J = 2, 3/2 \rightarrow 1, 1/2$ hfs transitions of CH near 2007 GHz discussed in Wiesemeyer et al. (2018) and Jacob et al. (2019). In Table 3 we present the derived ^{12}CH and ^{13}CH column densities using the same excitation conditions by adapting Eq. (5), as well as the resulting $^{12}\text{C}/^{13}\text{C}$ isotopic ratio. For W3(OH), towards which the ^{13}CH line remains undetected, we derive a 2σ lower limit on the $^{12}\text{CH}/^{13}\text{CH}$ abundance ratio of >58 over the velocity interval between -55 and -38 km s^{-1} .

The $^{12}\text{C}/^{13}\text{C}$ isotopic abundance ratio has been determined towards the GC region using a wide variety of molecules ranging from simple species such as CO, CN, H_2CO , and HCO^+ (Henkel et al. 1982; Langer & Penzias 1990; Savage et al. 2002) to more complex ones containing more than six atoms such as

$\text{CH}_3\text{CH}_2\text{CN}$, CH_3CCH , CH_2CHCN , and NH_2CHO (Belloche et al. 2016; Halfen et al. 2017), to name a few. The relatively lower values of the $^{12}\text{C}/^{13}\text{C}$ isotopic ratio towards the GC in comparison to the inner Galaxy, the local ISM, and the Solar System bears evidence to its advanced state of chemical evolution and reflects on its unique nucleosynthesis history. Moreover, the value of the GC strongly pivots the derived Galactic gradient. Therefore, as discussed by Halfen et al. (2017), it is essential to obtain more accurate measurements of the $^{12}\text{C}/^{13}\text{C}$ ratio towards the GC region because several of the derived molecular isotopic ratios can be hindered by effects of optical depth and saturation, chemical fractionation, and selective photo-dissociation. The limits on the $^{12}\text{C}/^{13}\text{C}$ isotopic ratio derived using CH are consistent with those derived by Savage et al. (2002) using CN for our sample of sources except for G34.26+0.15. The latter difference could be due to difficulties in deriving the ^{12}CN optical depth (i.e. an underestimation of the column density) because, as the authors of the above study state, the observed relative line intensity ratios of the hfs components does not follow LTE. The comparable isotopic compositions of the two molecular species stems from their inter-linked formation routes, as the neutral-neutral reaction between CH and N forms one of the main formation pathways for the production of CN ($\text{CH} + \text{N} \rightarrow \text{CN} + \text{H}$) with a forward-reaction rate of $\sim 6.7 \times 10^{-11} \text{ cm}^3 \text{ s}^{-1}$ for a temperature of 50 K. This suggests that CH similar to CN shows negligible amounts of fractionation. Furthermore, Halfen et al. (2017) estimated $^{12}\text{C}/^{13}\text{C}$ isotopic ratios between 19 and 33 using several different complex organic species and an average value of $\sim 24 \pm 9$ towards the 64 km s^{-1} component of the GC source Sgr B2(N). Within the errors, the average $^{12}\text{C}/^{13}\text{C}$ isotopic ratio derived by these authors is also consistent with the values derived from CH and CN. This presents solid evidence that the ^{13}C isotopic enrichment in more complex molecules must arise from progenitor molecules such as CH and CN because the ^{13}C substitution of complex species by simple ion-molecule exchange reactions is not as straightforward as that of simple molecules.

In general, almost all the PDR models studied by Röllig & Ossenkopf (2013) with varying physical parameters display a $^{12}\text{CH}/^{13}\text{CH}$ fractionation ratio that is enhanced at higher values of $A_v (\geq 1)$. The degree of fractionation is coupled with the FUV flux present in the models; the weaker the FUV flux, the higher the fractionation ratio. The $^{12}\text{C}/^{13}\text{C}$ isotopic ratios we derive from CH show no indication of an enhanced value in comparison to those derived from for example CN, as shown in Table 3 and therefore no signature of fractionation. This is because towards the SFRs towards which we detect both ^{12}CH and ^{13}CH , the absorption from both isotopologues primarily traces the extended envelopes of these regions, which are exposed to a significant UV field and whose densities have been estimated to be about 10^3 cm^{-3} on parsec scales for Sgr B2(M) and other regions (Schmiedeke et al. 2016; Wyrowski et al. 2016). This value is typical for translucent molecular clouds. The gas-phase carbon reservoir in such regions is predominantly in either its atomic or ionised form and not locked up in CO, which means that there is enough ^{13}C and $^{13}\text{C}^+$ present for ion-molecule exchange reactions to form ^{13}C -substituted CH.

The previously determined $^{12}\text{C}/^{13}\text{C}$ isotopic ratios suffer from large error bars that may either be due to opacity effects in the main isotopologue or due to other systematic effects. Therefore it is not clear whether the high dispersion in values between galactocentric radii of 4–8 kpc, corresponding to regions with the most molecular mass content in the Milky Way (except for the GC region), are due to actual cloud-cloud variations. If the

Table 3. Synopsis of the derived column densities and $^{12}\text{C}/^{13}\text{C}$ isotopic ratios.

Source	$\nu_{\min}-\nu_{\max}$ [km s $^{-1}$]	$N(^{13}\text{CH})$ [10^{13} cm $^{-2}$]	$N(^{12}\text{CH})$ [10^{13} cm $^{-2}$]	$^{12}\text{C}/^{13}\text{C}$	
				CH	CN ^(a)
Sgr B2(M)	40–90	$4.61^{+0.70}_{-0.71}$	$73.02^{+0.60}_{-0.68}$	$15.8^{+0.24}_{-0.24}$	>12
W51E	45–75	$1.77^{+0.20}_{-0.26}$	$66.36^{+3.30}_{-4.21}$	$37.5^{+0.61}_{-0.61}$	35 ± 12
G34.26+0.15	35–70	$0.20^{+0.01}_{-0.02}$	$9.38^{+0.78}_{-0.93}$	$47.0^{+0.45}_{-0.66}$	28 ± 4
W49(N)	–5–25	$0.68^{+0.11}_{-0.09}$	$22.87^{+3.56}_{-3.72}$	$33.6^{+0.75}_{-0.70}$	44 ± 22
W3(OH)	–55–(–38)	<0.11 ^(b)	$6.58^{+0.72}_{-1.35}$	>58	63 ± 16

Notes. ^(a)Values taken from Milam et al. (2005) and references therein. ^(b)The column density for the non-detection was derived using the 2σ rms of level.

spread is indeed due to opacity effects, then the ground-state rotational transitions of CH studied in this work, which are free from such effects, should be well suited to quantitatively constrain the $^{12}\text{C}/^{13}\text{C}$ ratio. By combining the $^{12}\text{C}/^{13}\text{C}$ ratio values derived using CH with those derived by Henkel et al. (1985), Langer & Penzias (1990), Wouterloot & Brand (1996)⁴, Milam et al. (2005), Giannetti et al. (2014), Ritchey et al. (2011), Halfen et al. (2017), and Yan et al. (2019) and carrying out a weighted least-squares fit (see Fig. 4), we derive a revised $^{12}\text{C}/^{13}\text{C}$ Galactic gradient of $^{12}\text{C}/^{13}\text{C} = 5.87(0.45) R_{\text{GC}} + 13.25(2.94)$, where the values in parentheses represent 1σ uncertainties. The addition of our CH data points plus those from Wouterloot & Brand (1996), Ritchey et al. (2011), Giannetti et al. (2014) and Yan et al. (2019) result in values for the best-fit slope and intercept that are within the combined uncertainties consistent with the values derived by Halfen et al. (2017). The small uncertainties of the CH data result in somewhat smaller formal uncertainties of the fitted values.

5. Conclusions

We reported the first detections of ^{13}CH in the ISM, namely towards the Sgr B2(M), G34.26+0.15, W49(N), and W51E massive SFRs in the Milky Way. Hyperfine structure transitions connecting sub-levels of the ^{13}CH $N, J = 2, 1/2$ and $1, 1/2$ Λ -doublet states with frequencies near 1997 GHz were observed in absorption using GREAT/SOFIA, which provides an avenue to observe frequency bands for which spectrally resolved observations were previously not possible with HIFI/Herschel or earlier missions. The detection of ^{13}CH along with observations of the main isotopologue CH towards the same sources opens a new, independent way for determinations of the $^{12}\text{C}/^{13}\text{C}$ isotopic abundance ratio across the Galaxy. We derive $^{12}\text{C}/^{13}\text{C}$ isotopic ratios for those of our target sources with a ^{13}CH detection and a lower limit for W3(OH) towards which we did not detect this isotopologue. Our values agree with previous determinations made using varied chemical species and in particular CN. Our observations do not indicate a possible enhancement in the $^{12}\text{C}/^{13}\text{C}$ ratio derived from CH as it traces the more diffuse and translucent regions of the ISM in which CO is not the main reservoir of carbon. Furthermore, as its abundance peaks in regions of high UV radiation, CH is relatively unaffected by

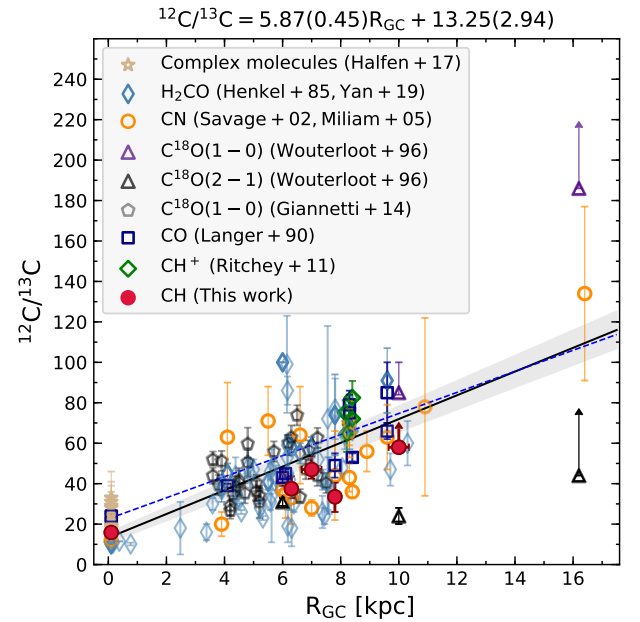


Fig. 4. Plot of $^{12}\text{C}/^{13}\text{C}$ isotope ratios as a function of galactocentric distance, R_{GC} (kpc). The filled red circles represent the $^{12}\text{C}/^{13}\text{C}$ ratio obtained using CH (this paper), while the empty black and purple triangles, grey pentagons, yellow circles, dark blue squares, and green, light blue diamonds and tan stars are those obtained using isotopologues of C^{18}O ($J = 1-0$ and $J = 2-1$ transitions) (Wouterloot & Brand 1996; Giannetti et al. 2014), CN (Savage et al. 2002; Milam et al. 2005), CO (Langer & Penzias 1990), CH^+ (Ritchey et al. 2011), H_2CO (Henkel et al. 1985; Yan et al. 2019), and complex organic molecules (Halfen et al. 2017), respectively. The black solid line represents the weighted fit to the data, and the grey shaded region demarcates the 1σ interval of this fit. For comparison, the fit obtained by Halfen et al. (2017) is displayed by the dashed blue line.

selective photo-dissociation and optical depth effects such as saturation. Hence, measurements of the $^{12}\text{C}/^{13}\text{C}$ isotopic ratio based on the fundamental rotational lines of CH potentially reflect the actual $^{12}\text{C}/^{13}\text{C}$ ratio in the gas.

In addition, knowledge of the ^{13}C substitution in CH will improve our understanding of interstellar chemistry because direct substitution of ^{13}C in more complex species is currently poorly understood and their observed $^{12}/^{13}\text{C}$ isotopologue ratios are speculated to originate in simpler precursors such as CH. Investigating a larger sample of SFRs at different galactocentric radii for ^{13}CH will allow for a better constraint on the average $^{12}\text{C}/^{13}\text{C}$ abundance ratio value in the ISM and on the Galactic

⁴ The authors of the cited article note that the discrepancy between the higher ratio derived from the $J = 1-0$ lines of $^{12}\text{C}^{18}\text{O}$ and $^{13}\text{C}^{18}\text{O}$ to the lower value from the $J = 2-1$ lines “is not yet explained, but may be due to the emission of the two transitions originating in different parts of the cloud with different excitation conditions.”

$^{12}\text{C}/^{13}\text{C}$ gradient, facilitating accurate Galactic chemical evolution models. However, the requirement of very high signal-to-noise ratios at high spectral resolutions that are required to detect the weak ^{13}CH absorption lines greatly restricts the selection of sources to those with strong continuum backgrounds for carrying out future follow-up studies. Furthermore, we hope that our study will encourage coordinated laboratory efforts resulting in refinements of the spectroscopic parameters of ^{13}CH , for which several of the constants describing the fine structure of its transitions, for instance, are not well established yet (Halfen et al. 2008).

Acknowledgements. We would like to thank David Neufeld and the anonymous referee for their valuable comments which helped to improve the clarity of this paper. SOFIA Science Mission Operations is jointly operated by the Universities Space Research Association, Inc., under NASA contract NAS2-97001, and the Deutsches SOFIA Institut under DLR contract 50 OK 0901 and 50 OK 1301 to the University of Stuttgart. upGREAT is financed by resources from the participating institutes, and by the Deutsche Forschungsgemeinschaft (DFG) within the grant for the Collaborative Research Center 956, as well as by the Federal Ministry of Economics and Energy (BMWi) via the German Space Agency (DLR) under Grants 50 OK 1102, 50 OK 1103 and 50 OK 1104. We are GREATful to the SOFIA operations team for their help and support throughout the course of the observations and after. The authors would like to express our gratitude to the developers of the many C++ and Python libraries, made available as open-source software, in particular this research has made use of the NumPy (van der Walt et al. 2011), SciPy (Jones et al. 2001) and matplotlib (Hunter 2007) packages.

References

- Bally, J., & Langer, W. 1982, *ApJ*, **255**, 143
- Belloche, A., Müller, H. S. P., Garrod, R. T., & Menten, K. M. 2016, *A&A*, **587**, A91
- Bergin, E. A., Phillips, T. G., Comito, C., et al. 2010, *A&A*, **521**, L20
- Bottinelli, S., Wakelam, V., Caux, E., et al. 2014, *MNRAS*, **441**, 1964
- Dagdigian, P. J. 2018, *MNRAS*, **475**, 5480
- Danks, A. C., Federman, S. R., & Lambert, D. L. 1984, *A&A*, **130**, 62
- Davidson, S. A., Evenson, K. M., & Brown, J. M. 2004, *J. Mol. Spectr.*, **223**, 20
- Dunham, T. 1937, *PASP*, **49**, 26
- Falgarone, E., Godard, B., Cernicharo, J., et al. 2010, *A&A*, **521**, L15
- Federman, S. R. 1982, *ApJ*, **257**, 125
- Gerin, M., de Luca, M., Goicoechea, J. R., et al. 2010, *A&A*, **521**, L16
- Giannetti, A., Wyrowski, F., Brand, J., et al. 2014, *A&A*, **570**, A65
- Godard, B., Falgarone, E., Gerin, M., et al. 2012, *A&A*, **540**, A87
- Godard, B., Falgarone, E., & Pineau des Forêts, G. 2014, *A&A*, **570**, A27
- Guan, X., Stutzki, J., Graf, U. U., et al. 2012, *A&A*, **542**, L4
- Halfen, D. T., Ziurys, L. M., Pearson, J. C., & Drouin, B. J. 2008, *ApJ*, **687**, 731
- Halfen, D. T., Woolf, N. J., & Ziurys, L. M. 2017, *ApJ*, **845**, 158
- Henkel, C., Wilson, T. L., & Bieging, J. 1982, *A&A*, **109**, 344
- Henkel, C., Guesten, R., & Gardner, F. F. 1985, *A&A*, **143**, 148
- Henkel, C., Wilson, T. L., Langer, N., Chin, Y. N., & Mauersberger, R. 1994, *Interstellar CNO Isotope Ratios*, (Berlin: Springer), 72, 439
- Herwig, F. 2005, *ARA&A*, **43**, 435
- Hierl, P. M., Morris, R. A., & Viggiano, A. A. 1997, *J. Chem. Phys.*, **106**, 10145
- Hunter, J. D. 2007, *Comput. Sci. Eng.*, **9**, 90
- Jacob, A. M., Menten, K. M., Wiesemeyer, H., et al. 2019, *A&A*, **632**, A60
- Jones, E., Oliphant, T., Peterson, P., et al. 2001, SciPy: Open source scientific tools for Python
- Kester, D., Higgins, R., & Teyssier, D. 2017, *A&A*, **599**, A115
- Klein, B., Hochgürtel, S., Krämer, I., et al. 2012, *A&A*, **542**, L3
- Langer, W. D., & Penzias, A. A. 1990, *ApJ*, **357**, 477
- Milam, S., Savage, C., Brewster, M., Ziurys, L. M., & Wyckoff, S. 2005, *ApJ*, **634**, 1126
- Neill, J. L., Bergin, E. A., Lis, D. C., et al. 2014, *ApJ*, **789**, 8
- Neufeld, D. A., Zmuidzinas, J., Schilke, P., & Phillips, T. G. 1997, *ApJ*, **488**, L141
- Neufeld, D. A., Godard, B., Gerin, M., et al. 2015, *A&A*, **577**, A49
- Ossenkopf, V., Röllig, M., Neufeld, I. A., et al. 2013, *A&A*, **550**, A57
- Pagel, B. 1997, *Nucleosynthesis and Chemical Evolution of Galaxies* (Cambridge: Cambridge University Press)
- Pickett, H., Poynter, R., Cohen, E., et al. 1998, *J. Quant. Spectr. Rad. Transf.*, **60**, 883
- Prantzos, N., Aubert, O., & Audouze, J. 1996, *A&A*, **309**, 760
- Qin, S.-L., Schilke, P., Comito, C., et al. 2010, *A&A*, **521**, L14
- Reid, M. J., Menten, K. M., Brunthaler, A., et al. 2014, *ApJ*, **783**, 130
- Richter, J., & Tonner, K.-F. 1967, *Z. Astrophys.*, **67**, 155
- Risacher, C., Güsten, R., Stutzki, J., et al. 2016, *A&A*, **595**, A34
- Ritchey, A. M., Federman, S. R., & Lambert, D. L. 2011, *ApJ*, **728**, 36
- Röllig, M., & Ossenkopf, V. 2013, *A&A*, **550**, A56
- Roueff, E., Loison, J. C., & Hickson, K. M. 2015, *A&A*, **576**, A99
- Rydbeck, O. E. H., Ellödér, J., & Irvine, W. M. 1973, *Nature*, **246**, 466
- Sato, M., Reid, M. J., Brunthaler, A., & Menten, K. M. 2010, *ApJ*, **720**, 1055
- Savage, C., Apponi, A. J., Ziurys, L. M., & Wyckoff, S. 2002, *ApJ*, **578**, 211
- Schmiedeke, A., Schilke, P., Möller, T., et al. 2016, *A&A*, **588**, A143
- Sheffer, Y., Rogers, M., Federman, S. R., et al. 2008, *ApJ*, **687**, 1075
- Stacey, G. J., Lugten, J. B., & Genzel, R. 1987, *ApJ*, **313**, 859
- Steimle, T. C., Woodward, D. R., & Brown, J. M. 1986, *J. Chem. Phys.*, **85**, 1276
- Swings, P., & Rosenfeld, L. 1937, *ApJ*, **86**, 483
- Tang, X. D., Henkel, C., Menten, K. M., et al. 2019, *A&A*, **629**, A6
- Tieftrunk, A., Pineau des Forêts, G., Schilke, P., & Walmsley, C. M. 1994, *A&A*, **289**, 579
- Tosi, M. 1982, *ApJ*, **254**, 699
- van der Walt, S., Colbert, S. C., & Varoquaux, G. 2011, *Comput. Sci. Eng.*, **13**, 22
- Watson, J. K. 2001, *ApJ*, **555**, 472
- Wiesemeyer, H., Güsten, R., Menten, K. M., et al. 2018, *A&A*, **612**, A37
- Wilson, T. 1999, *Rep. Prog. Phys.*, **62**, 143
- Wilson, T. L., & Rood, R. 1994, *ARA&A*, **32**, 191
- Wouterloot, J. G. A., & Brand, J. 1996, *A&AS*, **119**, 439
- Wyrowski, F., Güsten, R., Menten, K. M., et al. 2016, *A&A*, **585**, A149
- Xu, Y., Reid, M. J., Zheng, X. W., & Menten, K. M. 2006, *Science*, **311**, 54
- Yan, Y. T., Zhang, J. S., Henkel, C., et al. 2019, *ApJ*, **877**, 154
- Young, E. T., Becklin, E. E., Marcum, P. M., et al. 2012, *ApJ*, **749**, L17
- Zhang, B., Zheng, X. W., Reid, M. J., et al. 2009, *ApJ*, **693**, 419
- Zhang, B., Reid, M. J., Menten, K. M., et al. 2013, *ApJ*, **775**, 79

Appendix A: Sideband deconvolution

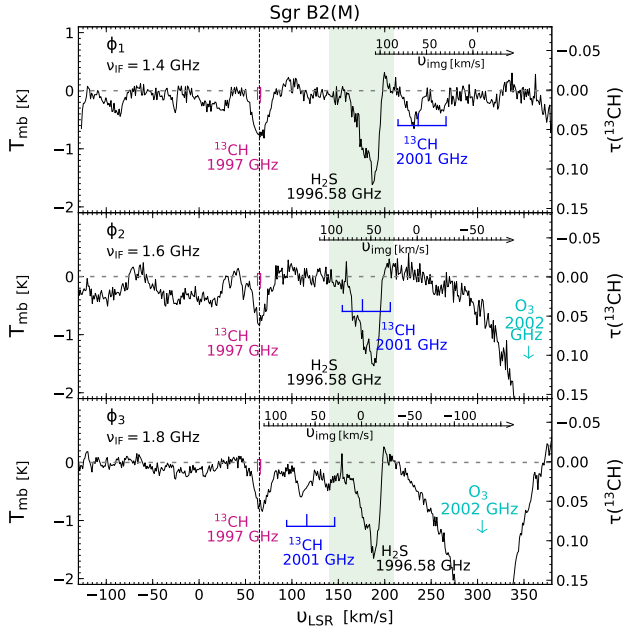


Fig. A.1. Calibrated and baseline-subtracted observed ^{13}CH spectra at an IF setting of 1.4 GHz (top panel), 1.6 GHz (central panel), and 1.8 GHz (bottom panel) towards Sgr B2(M). The secondary y-axis in each panel presents the optical depth scale. Signal bandpass contamination, possibly from the $J_{K^-,K^+} = 4_{3,2} \rightarrow 3_{2,1}$ transitions of H_2S at 1996.589 GHz, is displayed by the green shaded region. The hyperfine transitions corresponding to the 1997 GHz Λ -doublet arising from the signal band are displayed in pink, while that of the 2001 GHz Λ -doublet arising from the image band is displayed in blue. The change in IF pushes both the second Λ -doublet and the atmospheric ozone feature at 2002.347 GHz (telluric rest frame, marked in cyan) towards the signal band features. The secondary x-axis in each panel represents the image band LSR velocity scale.

In Fig. A.1 we display the ^{13}CH spectra towards Sgr B2(M) obtained from the different IF settings at 1.4, 1.6, and 1.8 GHz, respectively. The secondary x-axis displayed in each panel shows the velocity scale in the image band LSR. Each IF offset of 0.2 GHz corresponds to a shift of the image band features by 60 km s^{-1} . When an IF setting of 1.4 GHz is used, both sets of Λ -doublet features are well separated, with the hyperfine components corresponding to the 1997 GHz doublet originating from the signal band, while those corresponding to the 2001 GHz doublet arise from the image band. The ^{13}CH (signal band) Λ -doublet is seen in absorption, with a deeper absorption feature seen at 1996.589 GHz that possibly arises from the $J_{K^-,K^+} = 4_{3,2} \rightarrow 3_{2,1}$ transitions of H_2S . Several transitions of H_2S have previously been detected towards the Sgr B2(M) (Tieftrunk et al. 1994) and Sgr B2(N) (Neill et al. 2014) SFRs, with the higher frequency transitions typically seen in absorption towards the envelope of these hot cores. This transition lying close to 1996 GHz has previously not been detected using HIFI/Herschel because it lies outside the tuning range of HIFI Band 7. However, the $J_{K^-,K^+} = 6_{1,6} \rightarrow 5_{0,5}$ high-energy transition of H_2S at 1846.76 GHz with a lower level energy $\sim 239 \text{ K}$ was observed using HIFI/Herschel towards Sgr B2(M) as a part of the HIFI/Herschel observations of EXtra-Ordinary Sources (HEXOS; Bergin et al. 2010) guaranteed time key programme, which was aimed at investigating the chemical composition of several sources in the Orion and Sgr B2 SFRs. The spectrum of

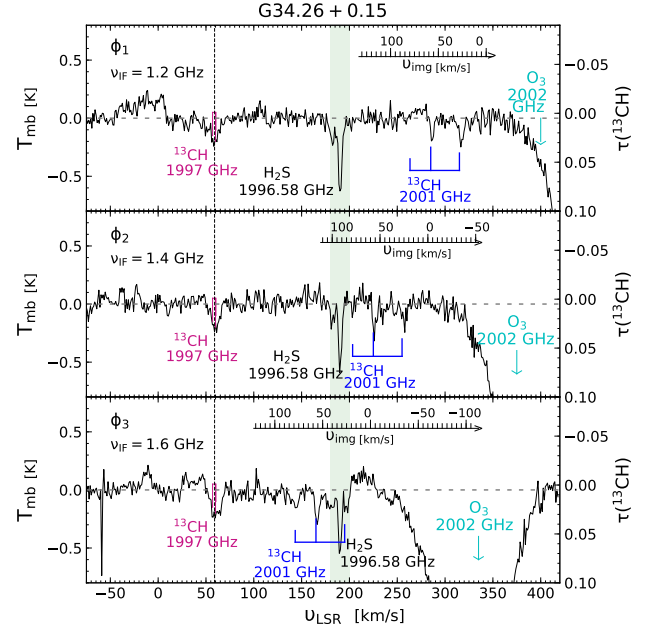


Fig. A.2. Same as Fig. A.1, but towards G34.26+0.15 for IF settings of 1.2, 1.4, and 1.6 GHz (from top to bottom).

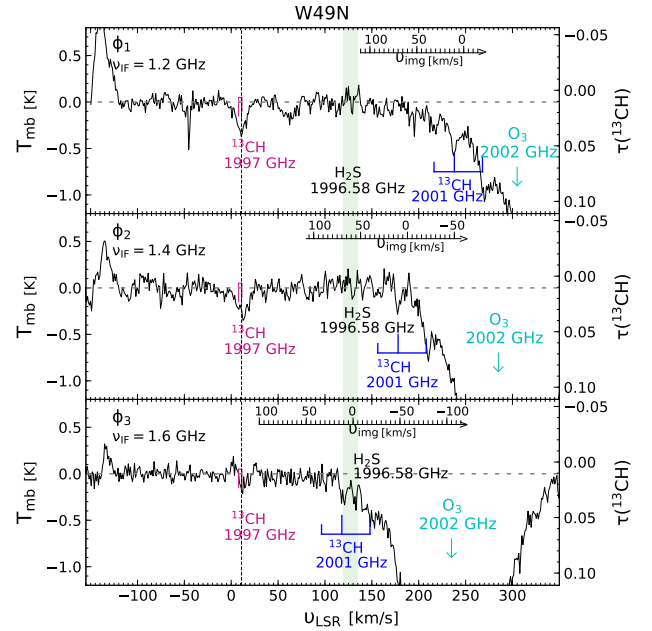


Fig. A.3. Same as Fig. A.1, but towards W49(N) for IF settings of 1.2, 1.4, and 1.6 GHz (from top to bottom).

H_2S near 1846.76 GHz observed towards Sgr B2(M) using HIFI (observation id 1342206640) shows an absorption profile which is similar to that of the signal-band feature we observed, with comparable line widths and peak temperatures, which further validates our assumption that this line arises from H_2S .

Despite pushing the 2001 GHz Λ -doublet transitions into the atmospheric ozone feature at 2002.347 GHz, the additional observing setup with an IF of 1.6 GHz was used to confirm the origin of the deeper absorption feature in the signal band. When we use this setup, it is clear that the deeper H_2S absorption feature must arise from the signal band while further confirming our detection of ^{13}CH absorption towards the envelope of the

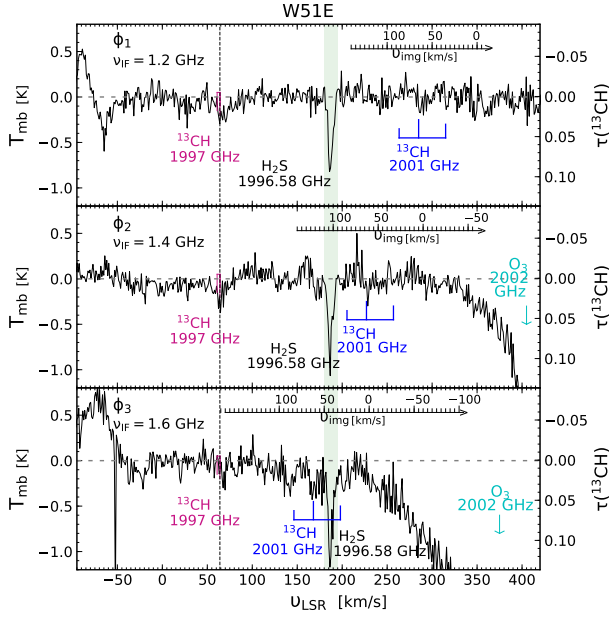


Fig. A.4. Same as Fig. A.1, but towards W51E for IF settings of 1.2, 1.4, and 1.6 GHz (from top to bottom).

SFR. However, we require a third IF setting in order to confirm the presence of weak sight-line absorption features. When the IF offset is increased to 1.8 GHz, the ^{13}CH features arising from the image band approach the ^{13}CH features arising from the signal band. We compare the average of the residuals between two independent IF settings with the average of the IF co-added spectrum. Whilst affirming the presence of weaker LOS absorption features by suppressing the image-band contributions, this does not present a complete DSB deconvolution. This can be mathematically formulated as described below.

We represent the DSB ^{13}CH spectrum obtained from each IF setting as a function of velocity as

$$\phi(v)_i = \phi_{\text{sig}}(v) + \phi_{\text{img}}(v_i - v), \quad (\text{A.1})$$

where $i = 1, 2, 3$ correspond to the different IF settings at 1.4, 1.6, and 1.8 GHz, respectively, v_i is the signal-band velocity at which the image-band velocity is equal to zero and ϕ_{sig} and ϕ_{img} represent the signal and image-band contributions. According to Eq. (A.1), the average of the IF co-added spectrum is

$$\phi(v)_{\text{avg}} = \phi_{\text{sig}}(v) + \frac{1}{3}(\phi_{\text{img}}(v_1 - v) + \phi_{\text{img}}(v_2 - v) + \phi_{\text{img}}(v_3 - v)). \quad (\text{A.2})$$

The set of independent residuals between the different IF settings using the spectrum with an IF = 1.4 GHz as reference is

$$\phi(v)_{1-2} = \phi(v)_1 - \phi(v)_2, \quad (\text{A.3})$$

$$\phi(v)_{1-3} = \phi(v)_1 - \phi(v)_3. \quad (\text{A.4})$$

The average of these residuals will reduce the image-band features from the spectra with IF settings 1.6 and 1.8 GHz by half,

$$\phi_{\text{residual-avg}} = (\phi(v)_{1-2} + \phi(v)_{1-3}) / 2 \quad (\text{A.5})$$

$$= (2\phi_{\text{img}}(v_1 - v) - \phi_{\text{img}}(v_2 - v) - \phi_{\text{img}}(v_3 - v)) / 2. \quad (\text{A.6})$$

Subtracting Eq. (A.6) from Eq. (A.2) yields

$$\phi_{\text{resultant}} = \phi_{\text{avg}} - \phi_{\text{residual-avg}} \quad (\text{A.7})$$

$$= \phi_{\text{sig}}(v) - \frac{2}{3}\phi_{\text{img}}(v_1 - v) + \frac{5}{6}\phi_{\text{img}}(v_2 - v) + \frac{5}{6}\phi_{\text{img}}(v_3 - v). \quad (\text{A.8})$$

While this exercise models the contribution of the 2001 GHz transitions of ^{13}CH , it does not confirm the profiles of the LOS features. Additionally, discrepancies in the noise level between the three spectral tunings arising from different integration times between them may lead to errors in the sideband reconstruction. However, the detection of ^{13}CH at the systemic velocity of the Sgr B2(M) molecular cloud remains undisputed.

A similar DSB deconvolution was carried out for G34.26+0.15, W49(N), and W51E using a nominal IF setting of 1.2, 1.2, and 1.4 GHz as reference, respectively. The spectra observed using each of the three different IF tunings towards each of these sources are displayed in Figs. A.2–A.4. We clearly detect the ^{13}CH 1997 GHz Λ -doublet component at the respective systemic velocities of G34.26+015, W49(N), and W51E in all three IF settings at 1.2, 1.4, and 1.6 GHz, but the hyperfine lines of the 2001 GHz Λ -doublet component either lie at the edge of the ozone feature for an IF setting of 1.2 GHz or move into the H_2S absorption feature for the higher IF tuning at 1.6 GHz. Although the detection of ^{13}CH towards the systemic velocities of these sources is confirmed, it is once again difficult to establish the presence of any LOS features after the sideband deconvolution.

Appendix B: ^{13}CH spectrum towards W3(OH)

In this appendix we display the ^{13}CH spectrum towards W3(OH).

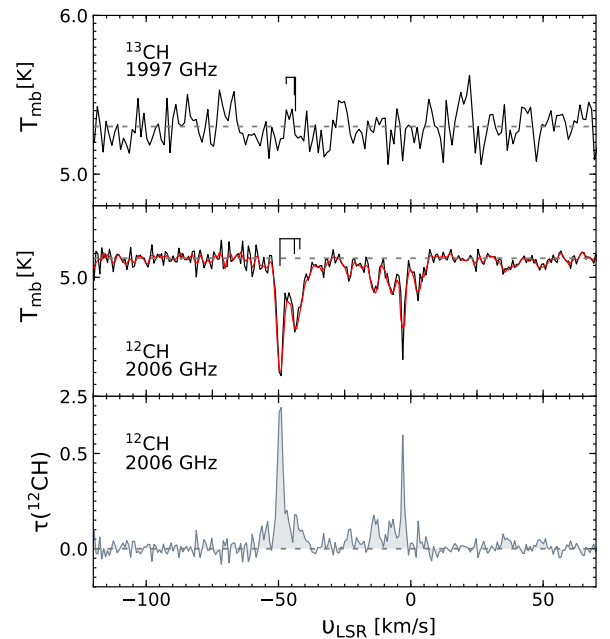


Fig. B.1. Spectra of the $N, J = 2, 3/2 \rightarrow 1, 1/2$ transitions of ^{13}CH near 1997 GHz (top) and CH near 2006 GHz (middle) observed towards W3(OH) in black. The Wiener filter model of the observed CH spectrum is overlaid in red. Bottom panel: Wiener filter deconvolved CH spectrum in optical depth scales.